Journal of Applied Polymer Science

# Two-stage drawing process to prepare high-strength and porous ultrahigh-molecular-weight polyethylene fibers: Cold drawing and hot drawing

**Hongli Liu,[1,2] Fei Lv,[2] Jing Li,[2] Tian Cao,[2] Caixia Wan,[2] Wenhua Zhang,[2] Liangbin Li,[2] Guoqiang Zheng,[1] Changyu Shen[1]**

[1]Key Laboratory of Advanced Material Processing and Mold (Ministry of Education), College of Materials Science and Engineering, Zhengzhou University, Zhengzhou 450001, China

[2]National Synchrotron Radiation Laboratory and College of Nuclear Science and Technology, Chinese Academy of Sciences Key Laboratory of Soft Matter Chemistry, University of Science and Technology of China, Hefei 230029, China

Correspondence to: W. Zhang (E-mail: zhangwh@ustc.edu.cn) and G. Zheng (E-mail: gqzheng@zzu.edu.cn)

**ABSTRACT:** High-strength and porous ultrahigh-molecular-weight polyethylene (UHMWPE) fibers have been prepared through a two-stage drawing process. Combined with tensile testing, scanning electron microscopy, and small-angle X-ray scattering, the mechanical properties, porosity, and microstructural evolution of the UHMWPE fibers were investigated. The first-stage cold drawing of the gel-spun fibers and subsequent extraction process produced fibers with oriented lamellae stacks on the surface and plentiful voids inside but with poor mechanical properties. The second-stage hot drawing of the extracted fibers significantly improved the mechanical properties of the porous fibers because of the formation of lamellar backbone networks on the surface and microfibrillar networks interwoven inside to support the voids. With various processing conditions, the optimized mechanical properties and porosity of the prepared UHMWPE fibers were obtained a tensile strength of 1.31 GPa, a modulus of 10.1 GPa, and a porosity of 35%. In addition, a molecular schematic diagram is proposed to describe structural development under two-stage drawing, including void formation and lamellar evolution. © 2015 Wiley Periodicals, Inc. J. Appl. Polym. Sci. **2015**, *132*, 42823.

**KEYWORDS:** morphology; polyolefins; porous materials; synthesis and processing; structure–property relations

Received 11 May 2015; accepted 8 August 2015
**DOI: 10.1002/app.42823**

## INTRODUCTION

Ultrahigh-molecular-weight polyethylene (UHMWPE) fibers have been widely applied in industrial, civil, sports, medical, military, and other fields because of its outstanding mechanical strength, impact resistance, abrasion resistance, self-lubrication, biocompatibility, and low-temperature resistance.[1–4] Recently, numerous innovative applications have surged out for UHMWPE fibers ranging from gas venting and air filtration to specialized separation and adsorption in harsh or corrosive environments.[5–7] These novel applications unanimously require a porous structure while retaining the high strength of the UHMWPE fibers to offer sufficient microchannels for mass transfer or large surface areas for adsorption.

Common methods for producing polymer fibers with a high porosity and high specific surface area rely on either the electrospinning of blends or thermal-induced phase separation.[7–11] Nevertheless, the fibers prepared in these ways always lack favorable mechanical properties.[7,12] In addition, Pennings and coworkers[13–16] prepared porous UHMWPE fibers, which were produced by the gel spinning of a semidilute solution of UHMWPE in paraffin oil followed by the extraction of paraffin oil in *n*-hexane. The obtained fibers were comprised of plentiful voids and lamellar stacks (or shish kebabs) but had a very low mechanical strength. Usually, an ultradrawing process is used to improve the mechanical strength of the fibers; these processes include cold drawing, hot drawing, local drawing, or multistage drawing. However, the porosity of the ultimate fibers in previous works appeared rather low, although a high strength and modulus were achieved.[13,16,17] Until now, related studies have placed almost all of their emphasis on the ultimate mechanical performance and mechanism of structural development of the UHMWPE fibers.[2,18–20] Little attention has been paid to the balance of the mechanical performance and porous structure or to the mechanism of void formation in porous UHMWPE fibers.

In this article, we describe a two-stage drawing process, namely, the first-stage cold drawing of gel-spun fibers followed by the extraction of paraffin oil to obtain oriented lamellae and a

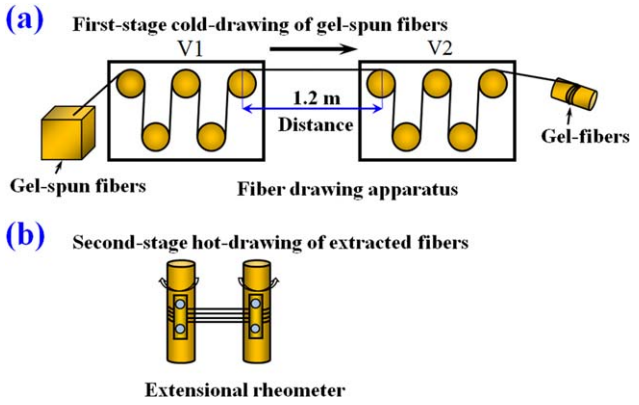


**Figure 1.** Schematic diagrams of the drawing apparatuses for (a) the first-stage cold-drawing process and (b) the second-stage hot-drawing process. V1 and V2 represent the rolling speed of the first group of five-roller and the second five-roller, respectively. [Color figure can be viewed in the online issue, which is available at wileyonlinelibrary.com.]

porous structure and the second-stage hot drawing of extracted fibers to enhance the mechanical properties, to prepare porous and high-strength UHMWPE fibers. Combined with scanning electron microscopy (SEM) and small-angle X-ray scattering (SAXS), the structural evolution and microscopic mechanism for void formation during the two-stage drawing of fibers were investigated. This study may afford some important parameters, such as the optimal draw temperature and draw ratio (DR) for manufacturing high-strength and porous UHMWPE fibers.

## EXPERIMENTAL

### Preparation of the Gel-Spun Fibers

The raw UHMWPE powder was kindly supplied by the Ningbo Institute of Industrial Technology with an average molecular weight of about 4 million. It was first dissolved in paraffin oil at a concentration of 5 wt %. To prevent the degradation of UHMWPE, 0.5 wt % antioxidant was added to the solution. Then, spinning was performed at 270°C on a TSE-35 corotating twin-screw extruder with an extrusion speed of 1 m/min. After spinning from the spinneret, the fibers were immediately quenched in cold water (10°C) and then collected through a take-up roller at a speed of 5 m/min. The obtained gel-spun fibers had a diameter of about 300 $\mu$m.

### First-Stage Cold Drawing of the Gel-Spun Fibers

A homemade fiber-drawing apparatus was used to perform the first-stage cold drawing of the gel-spun fibers at room temperature [first-stage draw temperature (T1) = 25°C]. The apparatus was comprised of two separate five-roller parts with a drawing distance of 1.2 m, as shown in Figure 1(a). By setting different rolling speeds (controlled by servo motors) for each part, we drew the gel-spun fibers at different strain rates [first-stage strain rate (SR1)] and draw ratios [first-stage draw ratio (DR1)]. The drawing parameters for the first-stage cold drawing of the gel-spun fibers are listed in Table I, where the corresponding sample array is named SR1–DR1. Note here that drawing with a DR1 higher than 10 could cause the fiber fracture. After the completion of drawing, the paraffin oil in the fibers was removed by ultrasonic extraction in an *n*-hexane bath; this was followed by a thorough drying in an oven.

**Table I.** First-Stage Cold-Drawing Parameters of the Gel-Spun Fibers

| Sample (SR1–DR1) | SR1 ($s^{-1}$) | DR1 | V1 (m/s) | V2 (m/s) |
|---|---|---|---|---|
| 0.1-3 | 0.1 | 3 | 0.06 | 0.18 |
| 0.1-5 | 0.1 | 5 | 0.03 | 0.15 |
| 0.1-10 | 0.1 | 10 | 0.013 | 0.13 |
| 0.5-10 | 0.5 | 10 | 0.067 | 0.67 |
| 1-10 | 1 | 10 | 0.133 | 1.33 |

V1 and V2 are the rolling speeds of the two groups of five-rollers as indicated in Figure 1(a).

### Second-Stage Hot Drawing of the Extracted Fibers

The second-stage hot drawing of the extracted fibers was carried out on a homemade two-drum extensional rheometer, as shown in Figure 1(b), which could heat the fibers homogenously by a hot nitrogen flow with a temperature fluctuation within ±0.5°C. The sample was secured on two geared drums by means of clamps. Drawing was carried out through the opposite rotation of geared drums driven by a servo motor. The second-stage strain rate (SR2) remained constant at 1 $s^{-1}$, and the other parameters in this drawing process are listed in Table II. For convenience, the samples with second-stage draw ratios (DR2s) of 1.5, 3, and 6 are marked A, B, and C, respectively, and the samples with second-stage draw temperatures (T2s) of 110, 120, 130, and 140°C are marked 1, 2, 3, and 4, respectively. Then, the total DR is defined as follows:

$$DR = DR1 \times DR2$$

### Tensile Testing

Tensile testing was conducted with a homemade miniature tensile tester at room temperature (25°C). A bundle of fibers were chosen to be measured to prevent possible error caused by a single fiber, and thus, an average stress value of the fibers was attained.[21] During tensile testing, fibers with an initial length

**Table II.** Second-Stage Hot-Drawing Parameters of the Extracted Fibers

| Sample | DR2 | DR | T2 (°C) |
|---|---|---|---|
| A1 | 1.5 | 15 | 110 |
| A2 | 1.5 | 15 | 120 |
| A3 | 1.5 | 15 | 130 |
| A4 | 1.5 | 15 | 140 |
| B1 | 3 | 30 | 110 |
| B2 | 3 | 30 | 120 |
| B3 | 3 | 30 | 130 |
| B4 | 3 | 30 | 140 |
| C1 | 6 | 60 | 110 |
| C2 | 6 | 60 | 120 |
| C3 | 6 | 60 | 130 |
| C4 | 6 | 60 | 140 |

**Table III.** Tensile Strength and Modulus of the Extracted Fibers

| Sample (SR1–DR1) | Tensile strength (GPa) | Modulus (GPa) |
|---|---|---|
| 0.1-3 | 0.02 | 0.25 |
| 0.1-5 | 0.025 | 0.38 |
| 0.1-10 | 0.07 | 0.46 |
| 0.5-10 | 0.1 | 0.69 |
| 1-10 | 0.17 | 0.86 |

($l_0$) of 4 mm was drawn at a constant tensile speed of 50 $\mu$m/s, and the tensile force ($F$) and displacement ($\Delta l$) of the fibers were recorded simultaneously. The engineering stress ($\sigma_e$) and engineering strain ($\varepsilon_e$) were calculated as follows:

$$\sigma_e = \frac{4F}{\pi D^2 N}, \quad \varepsilon_e = \frac{\Delta l}{l_0} \tag{1}$$

where $D$ is the average diameter of one single fiber and $N$ is the number of fibers within the bundle.

### SAXS Measurement

SAXS measurement was conducted at the BL16B beamline of the Shanghai Synchrotron Radiation Facility with an X-ray wavelength ($\lambda$) of 0.124 nm. A two-dimensional (2D) Mar165 CCD detector (2048 × 2048 pixels with a pixel size of 80 $\mu$m) was used to collect the scattering patterns. The distance between the sample and detector was 5360 mm calibrated by a standard sample (beef tendon). Fit2D software from the European Synchrotron Radiation Facility was used to analyze the SAXS patterns in terms of the scattering vector ($\mathbf{q} = 4\pi \sin\theta/\lambda$, where $2\theta$ is the scattering angle). Lorentz correction was applied to all of the one-dimensional (1D) intensity profiles.

### SEM

The surface and cross-sectional morphologies of fibers were observed by SEM (SIRION200). With regard to the cross-sectional preparation, the fibers were quenched to broken in liquid nitrogen. A small amount of Au was evaporated on the fibers before SEM observation.

### Porosity Determination

The relative volume of the voids in fibers was estimated to describe the porosity. First, the dry fibers were dipped in dimethyl benzene *in vacuo* until adsorption equilibrium was reached. Then, the wet fibers were taken out, and the residual solvent on the fiber surface was softly wiped up with filter paper. Finally, the fibers were weighed quickly. The porosity is defined as follows:

$$\text{Porosity } (\%) = \frac{(m_2 - m_1)\rho_p}{(m_2 - m_1)\rho_p + m_1\rho_x} \tag{2}$$

where $m_1$ is the weight of the dry fibers, $m_2$ is the weight of the wet fibers, $\rho_p$ is the density of UHMWPE (0.97 g/cm$^3$), and $\rho_x$ is the density of dimethyl benzene (0.86 g/mL). A similar method to calculate the porosity was also used in the study in ref. 22.

## RESULTS AND DISCUSSION

Table III shows the mechanical properties of the extracted fibers after the first-stage cold drawing of the gel-spun fibers. We found that both the tensile strength and modulus increased with SR1 and DR1; this indicated that increases in both SR1 and DR1 promoted the orientation of the molecular chains and the initial lamellae. It needs to be noted that no fiber fracture occurred in any of the tensile tests, even when the stretching length of the fibers reached the maximal allowable length of the tensile tester. Thus, the measured tensile strength was not the strength at break but a limited maximum strength. The low modulus showed that the fibers presented poor mechanical performance.

The surface and cross-sectional morphologies of the extracted fibers were observed by SEM, as shown in Figure 2. Sample 1-10 was selected as a representative because it presented the best mechanical properties. The fiber surface morphology shown in Figure 2(a) showed a hierarchical structure of loosely stacked lamellae oriented along the fiber axis; this was similar to the shish-kebab precursors on the as-spun fiber surface, as reported in ref. 23. Interestingly, the fiber cross section shown in Figure 2(b) displayed a skin–core structure where the thin skin layer exhibited agglomerated lamellar stacks, as shown in Figure 2(c). In contrast, a large number of voids with an average diameter of about 200 nm were formed at the core layer of the fiber, as shown in Figure 2(d). It is worth noting that this skin–core structure could have been formed during the gel-spun

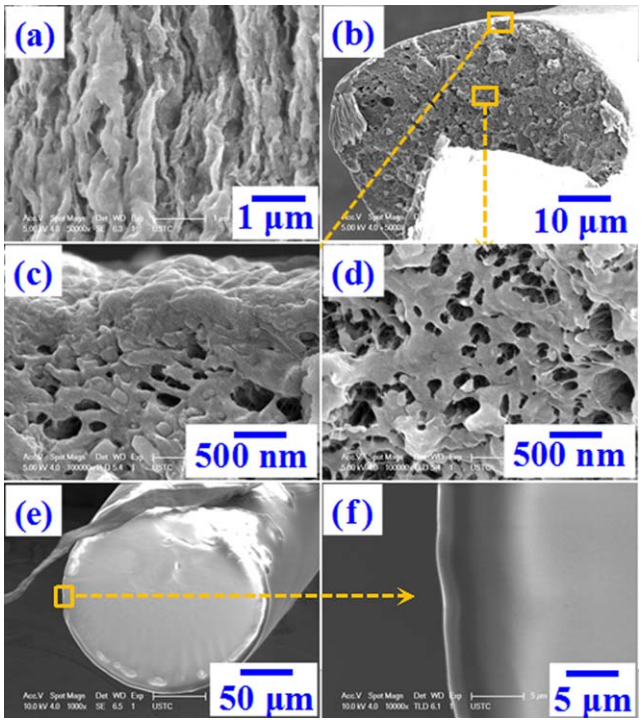


**Figure 2.** SEM micrographs of sample 1-10 after ultrasonic extraction: (a) fiber surface, (b) fiber cross section, (c) skin layer, (d) core layer of the cross section, (e) cross section of the gel-spun fiber, and (f) enlarged view of the yellow frame in panel e. [Color figure can be viewed in the online issue, which is available at wileyonlinelibrary.com.]

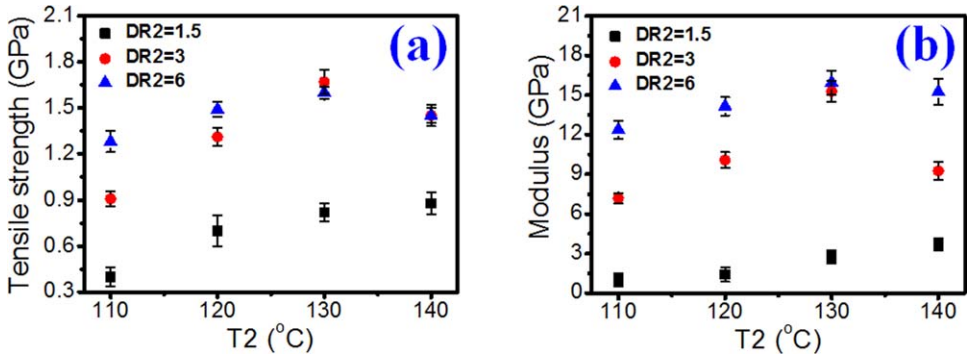


**Figure 3.** (a) Tensile strength and (b) modulus of fibers hot-drawn to different DR2s at different T2s. [Color figure can be viewed in the online issue, which is available at wileyonlinelibrary.com.]

process before cold drawing. For comparison, the cross-sectional morphology of the gel-spun fiber is also displayed in Figure 2(e). The fiber seemed to present a skin–core contour with a skin layer of about 20 $\mu$m. As shown by the enlarged view in Figure 2(f), the skin layer was actually fulfilled with paraffin oil and had a similar morphology in the core layer; this suggested the absence of the skin–core structure as in the extracted fibers. The skin–core structure in the extracted fibers was explained by the distribution of paraffin oil in the fibers. During the cold-drawing process, the paraffin oil close to fiber surface preferred to be squeezed out; this caused an agglomeration of molecular chains and lamellae to form a relatively compact skin layer. Thus, it was difficult for the paraffin oil that was retained in the interior of the fibers to flow out through the dense surface. With the subsequent extraction of paraffin oil by *n*-hexane, the original occupation filled by paraffin oil was replaced by the voids. The porosity of sample 1-10 was calculated to be about 54.8%; this was much higher than that of the UHMWPE fibers that were directly subjected to extraction followed by the hot-drawing process.[13]

With a combination of the SEM images in Figure 2, the poor mechanical properties of the extracted fibers after cold drawing were attributed to two points: one was the amorphous molecular chains and the weakly oriented lamellae along the fiber axis, and the other was the high porosity after extraction, which led to a low bulk density of fibers, namely, a loose structural arrangement. Therefore, it was necessary to perform further hot drawing of the extracted fibers to improve their mechanical properties.

It is known that the hot drawing of fibers can greatly enhance their mechanical strength through the production of a microfibrillar structure and an increase in the bulk density.[13,24] To obtain porous fibers with optimal strength and porosity, we carried out the second-stage hot drawing of extracted fibers by regulating the DRs (DR2 = 1.5–6) and the temperatures (T2 = 110–140°C; the melting range of the extracted fibers was approximately 95–145°C, and the melting point was about 133°C determined by differential scanning calorimetry at a heating rate of 10°C/min). The tensile strength and modulus of the hot-drawn fibers are displayed in Figure 3. Figure 3(a) shows that the tensile strength of the hot-drawn fibers increased at a higher DR2. At draw temperatures of 130 and 140°C, the tensile strength tended to be identical for DRs of 3 and 6. In addition, the tensile strength intensified with increasing T2 before 130°C. At a T2 of 140°C, the tensile strength appeared to drop slightly. Figure 3(b) shows the dependence of the modulus on T2 and SR2, and it presented similar results as the tensile strength. The increment of the mechanical properties of the fibers with DR2 was associated with the lamellar transformation to a microfibrillar structure; this will be further discussed later. The drop in the mechanical properties at a T2 higher than 130°C was mainly due to the melting of fibers at draw temperatures higher than the melting point.

To analyze the microstructural evolution of the hot-drawn fibers, the corresponding 2D SAXS patterns are shown in Figure 4. Sample S1, named after sample 1-10 heated up to 110°C and kept there for 5 min (DR2 = 0), exhibited a strong but dispersive elliptical SAXS pattern with a long axis perpendicular to the fiber axis. The elliptical pattern indicated a weak orientation of lamellar stacks, and the strong scattering intensity mainly resulted from the voids in the fibers. For all of the hot-drawn fibers, equatorial (vertical direction) streaks across the beam stop were observed; this indicated the existence of microfibrils or void structures in the fibers.[17] The meridional (horizontal direction) rodlike maxima along the drawing direction on both sides of beam stop were associated with the presence of well-defined lamellar stacks.[25,26] As hot drawing proceeded at a constant T2, the equatorial streak became more slender with increasing DR2; this was accompanied by a pair of weaker meridional maxima. This result clearly suggests a transformation from chain-folded lamellae to microfibrillar structures during hot drawing. With increasing T2 from 110 to 140°C at a fixed DR2, the equatorial streak appeared to weaken gradually; this suggested an accelerated collapse of microfibrils or a reduction of voids in the fibers.[17] Moreover, the meridional maxima gradually moved closer to the beam stop, manifesting a larger long period of lamellar stacks at higher T2. It needs to be pointed out that the change in the scattering intensity among different samples can also be influenced by the variance of samples, such as the different volume penetrated by X-ray. The detailed microstructural evolution of lamellae and voids in fibers will be discussed separately in the following.

The scattering vectors along and perpendicular to the drawing direction are defined as $\mathbf{q}_1$ and $\mathbf{q}_2$, respectively. To describe the

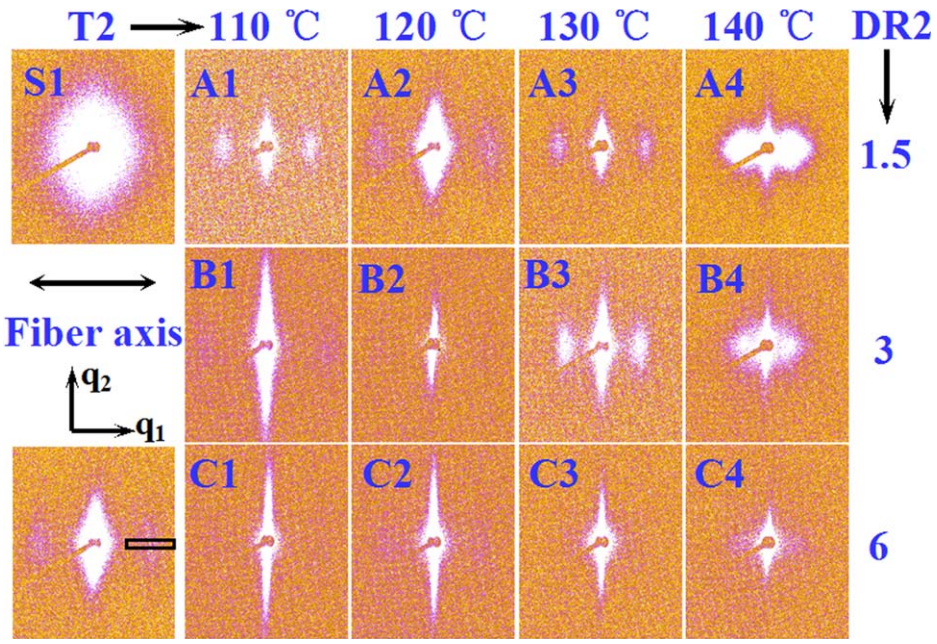


**Figure 4.** 2D SAXS patterns for fibers hot-drawn to different DR2s at different T2s. The drawing direction was horizontal. [Color figure can be viewed in the online issue, which is available at wileyonlinelibrary.com.]

oriented lamellar structure, the scattering intensity distribution [$I(\mathbf{q}_1)$] was obtained by meridian scanning with a certain width along the equatorial direction, as schematically shown in the lower left panel of Figure 4. Figure 5 shows the profiles of $I(\mathbf{q}_1)$ for fibers under different drawing conditions. The lamellar long period ($L_{ac}$) is defined as follows:

$$L_{ac} = L_c \times L_a$$

where $L_c$ and $L_a$ are the average thicknesses of the crystalline and amorphous layers, respectively. $L_{ac}$ was calculated with the equation $L_{ac} = 2\pi/\mathbf{q}_{1\max}$ on the basis of Bragg's law, where $\mathbf{q}_{1\max}$ is the peak position of $I(\mathbf{q}_1)$. The fibers hot-drawn at 110°C were selected as representative to describe the lamellar evolution at

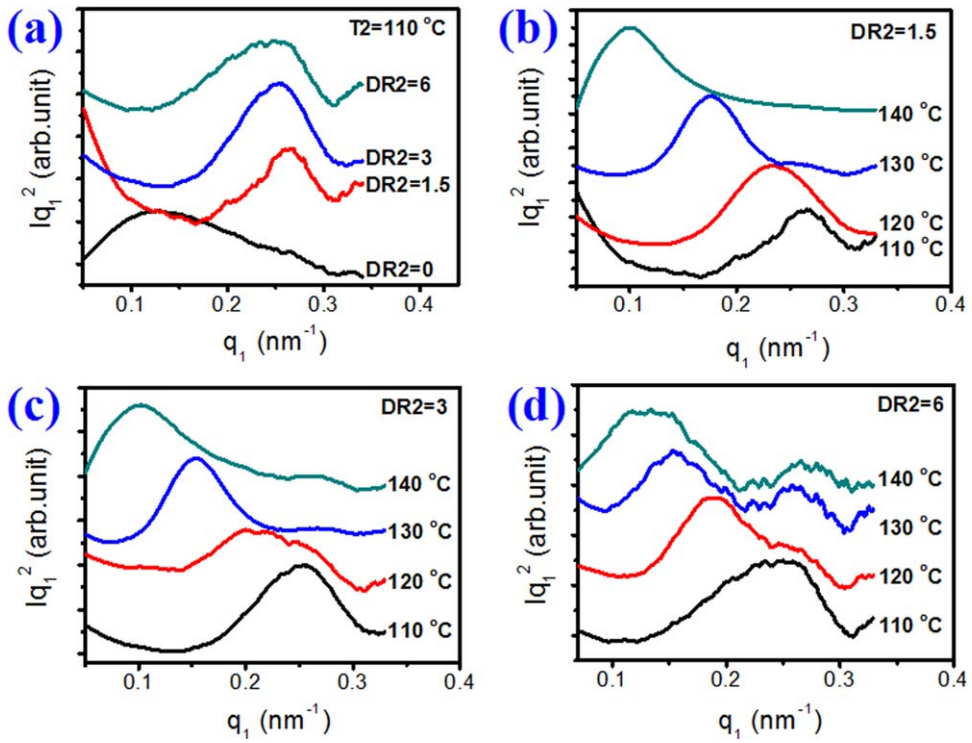


**Figure 5.** 1D SAXS intensity profiles along the meridian for fibers hot-drawn (a) to different DR2s at T2 = 110°C and (b) to DR2 = 1.5, (c) to DR2 = 3, and (d) DR2 = 6 at different T2s. [Color figure can be viewed in the online issue, which is available at wileyonlinelibrary.com.]

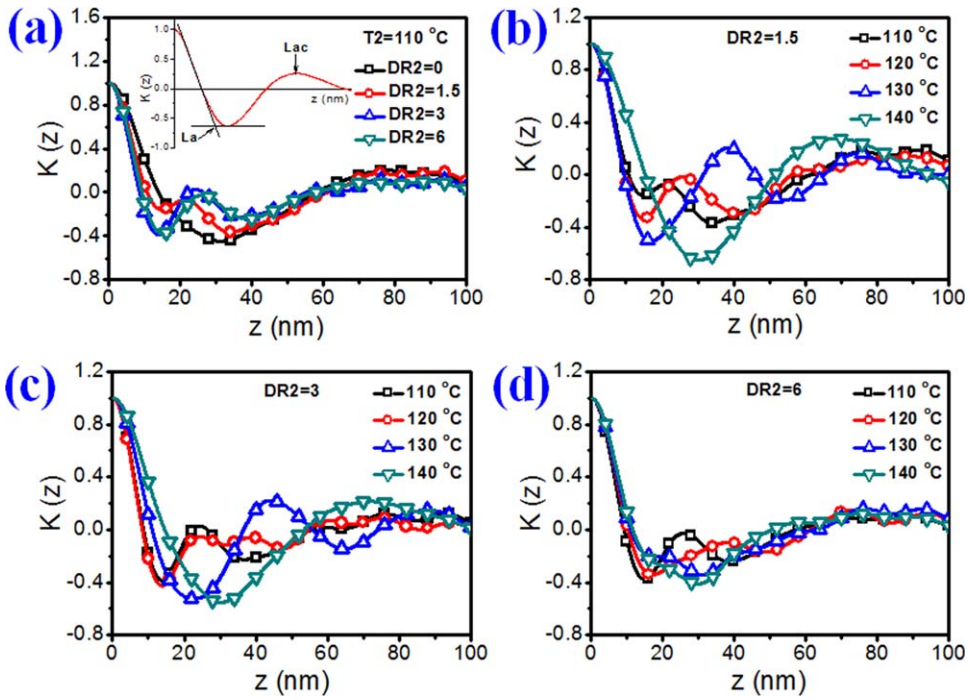


**Figure 6.** 1D correlation function $K(z)$ for fibers hot-drawn (a) to different DR2s at T2 = 110°C and (b) to DR2 = 1.5, (c) to DR2 = 3, and (d) to DR2 = 6 at different T2s. [Color figure can be viewed in the online issue, which is available at wileyonlinelibrary.com.]

different DR2s because the development tendencies of SAXS patterns for fibers drawn at different T2 (except for 140°C) were similar, as shown in Figure 4. As shown in Figure 5(a), $\mathbf{q}_{1\max}$ showed an obvious increase from 0.12 $nm^{-1}$ (DR2 = 0) to 0.26 $nm^{-1}$ (DR2 = 1.5) at the initial drawing stage. Upon further drawing, almost no change in $\mathbf{q}_{1\max}$ occurred; this suggested a nearly constant long period. In addition, Figure 5(b–d) shows the $I(\mathbf{q}_1)$ curves at different DR2, which were varied over T2.

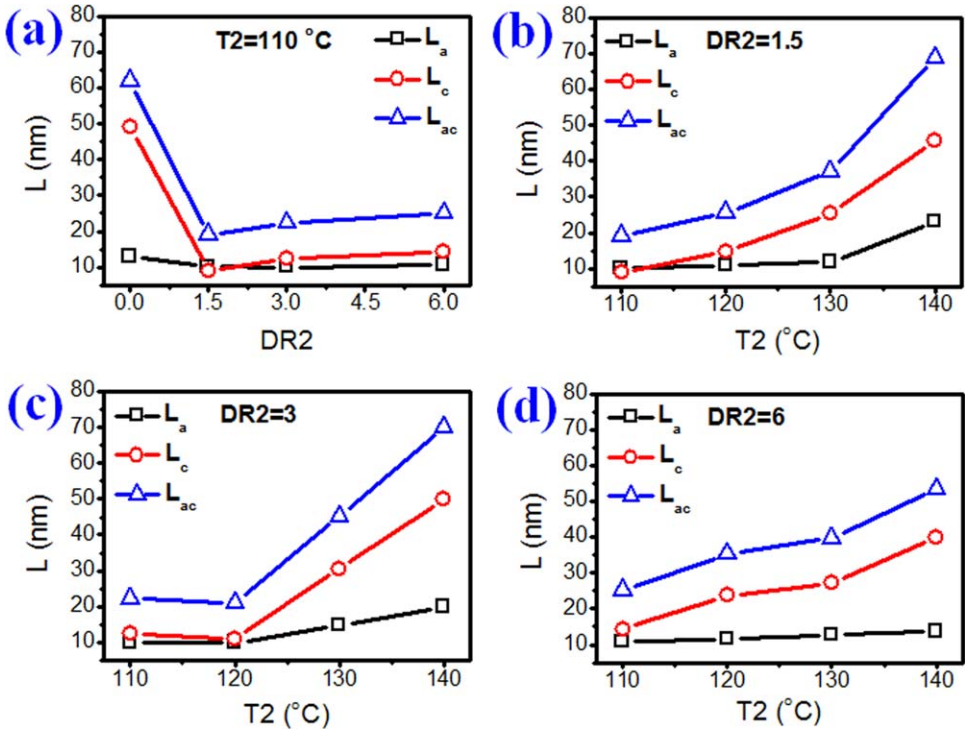


**Figure 7.** Long period ($L_{ac}$), lamellar thickness ($L_c$), and amorphous thickness ($L_a$) of fibers hot-drawn (a) to different DR2s at T2 = 110°C and (b) to DR2 = 1.5, (c) to DR2 = 3, and (d) to DR2 = 6 at different T2s. The ordinate $L$ indicates the dimensional size of each microstructural units. [Color figure can be viewed in the online issue, which is available at wileyonlinelibrary.com.]

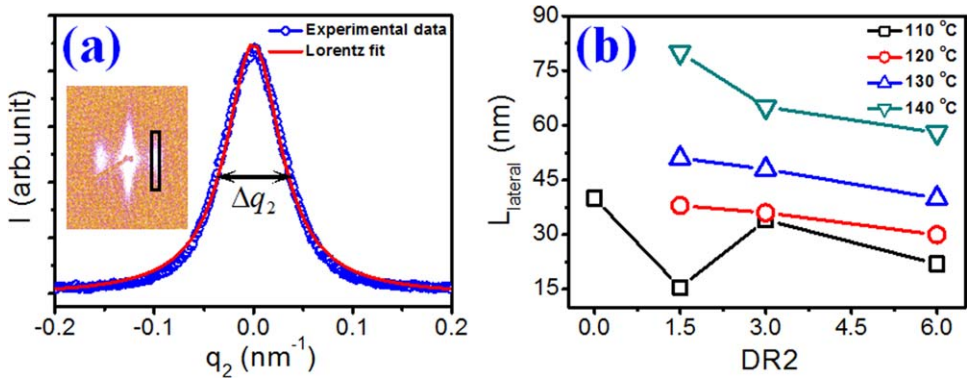


**Figure 8.** (a) Fitting process of $L_{lateral}$ of lamellae and (b) $L_{lateral}$ of the lamellae as a function of DR2 for fibers drawn at different T2s. [Color figure can be viewed in the online issue, which is available at wileyonlinelibrary.com.]

We found that a higher T2 always led to a smaller $\mathbf{q}_{1max}$; this suggested a positive dependence of $L_{ac}$ on T2.

$L_c$ and $L_a$ were further calculated from the 1D correlation function $[K(z)]$ of the electron density $(\rho)$ distribution in lamellar stacks as follows:[27–29]

$$K(z)=\frac{\int_0^\infty I(\mathbf{q}_1)\cos(\mathbf{q}_1 z)d\mathbf{q}_1}{\int_0^\infty I(\mathbf{q}_1)d\mathbf{q}_1} \quad (3)$$

where $z$ is the drawing direction. Figure 6 shows the 1D correlation functions along the drawing direction $z$ for fibers under different drawing conditions. The inset in Figure 6(a) shows how $L_a$ and $L_{ac}$ were derived. The average thickness of the crystalline layer is then given as $L_c = L_{ac} - L_a$.

Figure 7(a) presents that $L_{ac}$ decreased significantly from 62 to 20 nm; this was accompanied by a coincident decrease in $L_c$ when samples were drawn to a low DR of 1.5. Such a sharp change was attributed to the breakage and reorganization of the initial lamellae caused by the drawing stress. As shown by the SEM micrographs (Figure 2) and SAXS pattern (Figure 4), sample S1 (DR2 = 0) was composed of weakly oriented lamellar stacks; these were apt to slip and break, disintegrating into smaller blocks (new lamellae), when they could not endure the drawing stress with increasing DR2. The resulting new lamellar stacks presented a closer packing, and this improved the mechanical strength of the fibers. With further increases in DR2, the equatorial streak in the SAXS pattern (Figure 4) became more slender; this implied the formation of abundant microfibrillar structures, as discussed previously. Thus, the subsequent negligible increase in $L_{ac}$ (<10 nm) was probably the result of microfibril slipping. The formation of microfibrils significantly improved the mechanical properties of the fibers.

Figure 7(b–d) shows that $L_{ac}$ and $L_c$ displayed the same increasing trend with increasing draw temperature. This was attributed to the influence of the temperature on the drawing-induced breakage and recrystallization. The newly formed lamellae obtained a more perfect structure with a higher thickness at a higher temperature; this was similar to the effect of annealing. In addition, $L_{ac}$ of the fibers drawn to lower DR2 was more sensitive to the draw temperature than that of the fibers drawn to a higher DR2, because the increasing trend of $L_{ac}$ with the draw temperature became slower when DR2 was increased.

According to the deformation behaviors of the long period and the thickness of the lamellae, the lateral size ($L_{lateral}$) of the lamellae should have also changed during the structural evolution. $L_{lateral}$ was derived from the full width at half-height ($\Delta\mathbf{q}_2$) of the scattering peak in the equatorial direction according to $L_{lateral} = 2\pi/\Delta\mathbf{q}_2$, as shown in Figure 8(a). Figure 8(b) shows that $L_{lateral}$ of the lamellae decreased generally with increasing DR2 for fibers at a constant T2. The variation of $L_{lateral}$ was in accordance with the breakage of large lamellae and the transformation from lamellae to microfibrils.

In this study, a large number of voids were proven to be retained during the hot-drawing process; this was supported by three facts. First, according to the SAXS principles, the integrated invariant of the equatorial streak ($Q$) was evaluated as follows:[30,31]

$$Q=\frac{1}{2\pi^2}\int_0^\infty q^2 I(q)dq = V^2\langle\rho^2\rangle \quad (4)$$

Here, $Q$ is only correlated with the volume ($V$) of the scattering subject and the difference of the electronic density ($\rho$). In PE, $(\rho_c - \rho_a)^2 \approx 6.7 \times 10^{-3}$ mol$^2$ electron$^2$/cm$^6$, $(\rho_c - \rho_v)^2 \approx 3.26 \times 10^{-1}$ mol$^2$ electron$^2$/cm$^6$, and $(\rho_a - \rho_v)^2 \approx 2.39 \times$

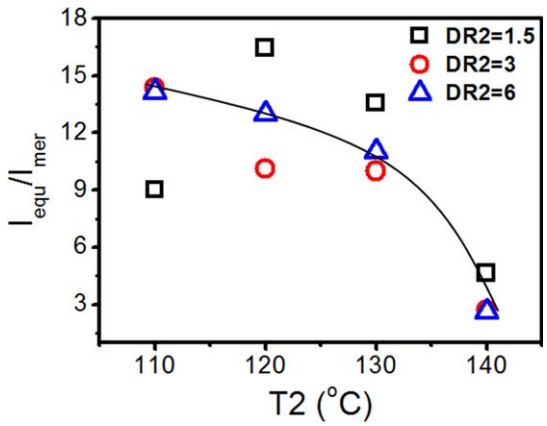


**Figure 9.** Relative intensity of $I_{equ}/I_{mer}$ for fibers hot-drawn to different DR2s at different T2s. $I_{equ}$ and $I_{mer}$ are the scattering intensity of the equatorial streak and the meridional maxima, respectively. [Color figure can be viewed in the online issue, which is available at wileyonlinelibrary.com.]

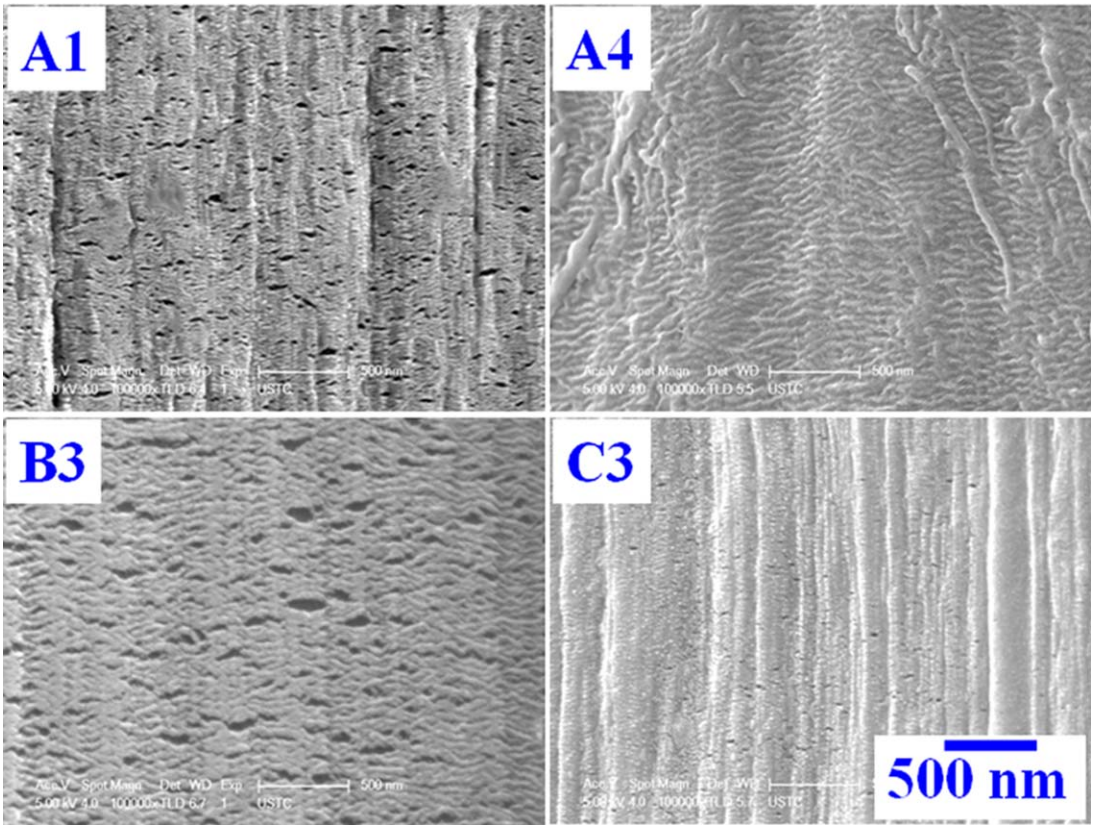


**Figure 10.** SEM surface micrographs of the hot-drawn fibers. [Color figure can be viewed in the online issue, which is available at wileyonlinelibrary.com.]

$10^{-1}$ mol$^2$ electron$^2$/cm$^6$; $\rho_a$, $\rho_c$ and $\rho_v$ are the electronic density of the amorphous phase, crystalline phase and the voids, respectively.[16] The $\rho$ difference between the voids and amorphous phase or crystalline phase was approximately 30–50 times larger than that between the amorphous phase and the crystalline phase; this implied that the scattering intensity was much more dependent on the formation of voids in fibers. Therefore, the content of voids was estimated from the strong scattering intensity of the equatorial streak ($I_{equ}$). Taking into account the diversity among the samples in our experiment, a relative scattering intensity ($I_{equ}/I_{mer}$, where $I_{mer}$ is the intensity of the meridional maxima) was proposed to reflect the relative content of the voids. Figure 9 shows that $I_{equ}/I_{mer}$ decreased obviously with increasing T2. The rapid decline of $I_{equ}/I_{mer}$ at 140°C was in agreement with the lamellae melting and resulted in the significant reduction of voids at excessively high temperatures. In addition, the dependence of $I_{equ}/I_{mer}$ on DR2 was small.

Second, the existence of voids in the hot-drawn fibers was directly verified by SEM observation, as shown in Figure 10. An obvious shish-kebab structure presented on the sample A1 (110°C) surface, where kebabs were stacked so densely that no shish was observed. Among the kebabs, a great deal of voids were formed with an average size of about 100 × 30 nm$^2$. For sample A4 (140°C), the fiber surface was covered by thick lamellar stacks, and no voids survived; this was also ascribed to

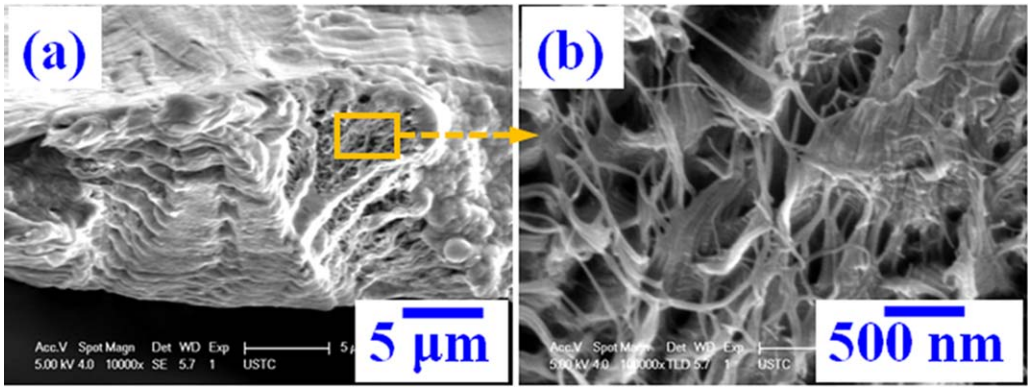


**Figure 11.** (a) SEM cross-sectional micrograph of the hot-drawn fibers and (b) magnification of the yellow frame shown in panel a. [Color figure can be viewed in the online issue, which is available at wileyonlinelibrary.com.]

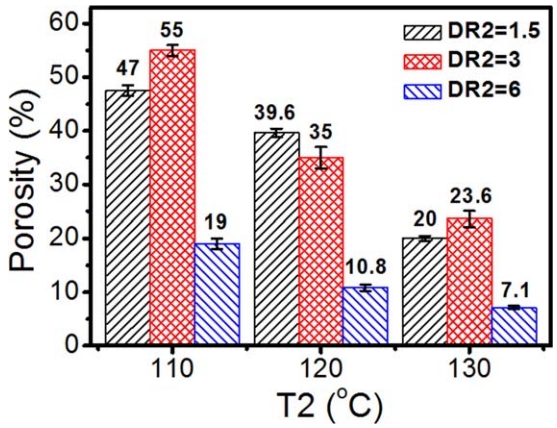


**Figure 12.** Porosity of the fibers hot-drawn to different DR2s as a function of T2. [Color figure can be viewed in the online issue, which is available at wileyonlinelibrary.com.]

the melting of the lamellae at temperatures higher than the melting point. In a comparison of samples B3 and C3, the surface morphologies were quite different, although they had similar mechanical properties (Figure 3). The surface of sample B3 was composed of lamellar stacks aligned normal to the fiber axis, among which abundant ellipsoidal voids were formed, whereas the surface of sample C3 showed a distinctly microfibrillar structure composed of narrow lamellae and only small voids dispersed sporadically. It was reasonable that for sample B3, the overgrowth of chain-folded lamellae prevented close packing of the backbone fibrils; this led to a porous structure. As DR was large enough (sample C3), the folded-chain lamellae transformed into a microfibrillar structure because of the large drawing stress. At the same time, the microfibril slipping caused a close packing of the microfibrillar structure and resulted in a sharp decrease in the voids.

Figure 11 further displays the cross-sectional micrographs of the hot-drawn fiber. In Figure 11(a), the strong backbone networks of large lamellar stacks, undertaking a high mechanical strength for the fiber, are shown clearly in the cross section of fiber. Actually, the backbone networks were filled with porous fibrillar networks interwoven together by slim microfibrils, as shown in Figure 11(b); this gave rise to a high porosity and high specific surface area for the fiber. This exquisite configuration is expected to give a high potential for applications in harsh or corrosive environments, such as uranium extraction from seawater or heavy-metal extraction from rivers and lakes.

Finally, the porosity of the hot-drawn fibers was quantitatively measured, and the results are shown in Figure 12. The fibers drawn at 140°C were not considered because of the apparent melting on surface. At a constant DR2, the porosity decreased with increasing T2. In fact, it showed a contradictory relationship between the porosity and the mechanical strength. Although the fibers drawn at 130°C had the best mechanical properties (see Figure 3), they lost much of their porosity. It seemed that the optimized mechanical strength and porosity of the fibers were obtained at a DR2 of 3 and a T2 of 120°C. Under these conditions, the tensile strength was 1.31 GPa, the modulus was 10.1 GPa, and the corresponding porosity was 35%. The best processing parameters for gaining compromised mechanical properties and porosity in the UHMWPE fibers depended on the specific requirement of the fibers' performance. Our experimental results in this study are of significance in affording a narrow scope for seeking the optimization of the UHMWPE process for both a high mechanical strength and a considerably large porosity.

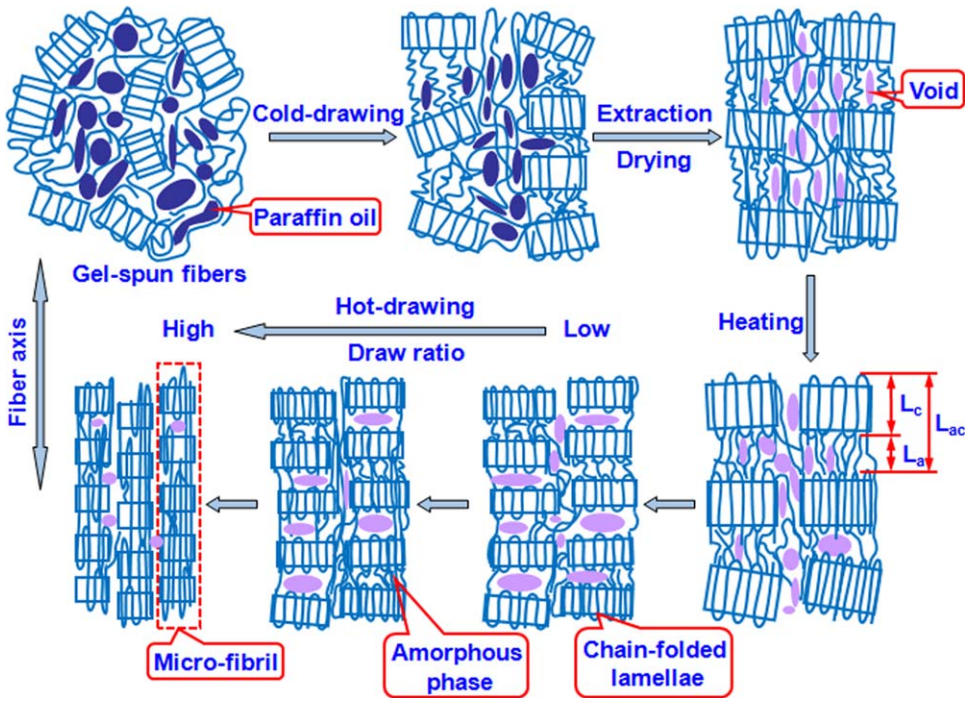


**Figure 13.** Schematic diagram of the microstructural evolution of the fibers during the first-stage cold-drawing process and second-stage hot-drawing process. [Color figure can be viewed in the online issue, which is available at wileyonlinelibrary.com.]

On the basis of the previous experimental results and analysis, a schematic diagram is proposed to describe the microstructural evolution of fibers during drawing, as shown in Figure 13. In the first-stage cold drawing of gel-spun fibers, the amorphous molecular chains and initial lamellae gained a certain orientation degree under the lubrication of paraffin oil. Then, a skin–core structure occurred with a hierarchical structure of loosely oriented lamellar stacks on the surface and abundant voids inside after the extraction and drying process. Before the second-stage hot drawing, the fibers were heated to T2, during which the lamellae were regularized because of the reduction of defects and the improvement of the chain arrangement. As the second-stage hot drawing proceeded to a low DR, the oriented large lamellae broke and reorganized to form new thin lamellae under the drawing stress. In this stage, voids survived among the lamellar stacks. Upon further drawing, the folded-chain lamellar stacks gradually transformed into a microfibrillar structure because of the larger drawing stress. The dense alignment of microfibrils resulted in a significant decrease in the porosity of the fibers. In addition, when the draw temperature increased beyond 130°C, the melting and recrystallization process dominated, and this led to the destruction of the voids.

## CONCLUSIONS

High-strength and porous UHMWPE fibers were prepared by a two-stage drawing process. The mechanical strength and porosity, together with the microstructural evolution during the drawing were investigated by virtue of tensile testing, SEM, and SAXS characterization. During the first-stage cold drawing of the gel-spun fibers, the strain rate and DR were positive in promoting the orientation of amorphous molecular chains and initial lamellae. The subsequent extraction and drying process produced a skin–core structure of fibers with loosely oriented lamellar stacks on the surface and plentiful voids inside; it showed poor mechanical properties. In the second-stage hot drawing of extracted fibers, suitable increases in DR and draw temperature significantly improved the mechanical properties, despite somewhat of a reduction in the porosity, because of the formation of lamellar networks on the surface and porous interwoven fibrillar networks inside. With the balance between the mechanical properties and porosity of the fibers, the prepared UHMWPE fibers presented an optimal tensile strength of 1.31 GPa, a modulus of 10.1 GPa, and a porosity of 35% under two-stage drawing: cold drawing at a strain rate of 1 $s^{-1}$ to a DR of 10 followed by hot drawing at a strain rate of 1 $s^{-1}$, a draw temperature of 120°C, and a DR of 3.

## ACKNOWLEDGMENTS

The authors acknowledge Prof. Peng Chen's group (Ningbo Institute of Industrial Technology, Chinese Academy of Sciences) for supplying the UHMWPE powder and helping with the spinning of the UHMWPE gel-spun fibers. They also acknowledge the Shanghai Synchrotron Radiation Facility for the provision of synchrotron beam time. This work was supported by the National Natural Science Foundation of China (contract grant numbers 51227801 and 51325301) and the Fundamental Research Funds for the Central Universities.

## REFERENCES

1. Wyatt, T.; Deng, Y.; Yao, D. *Polym. Eng. Sci.* **2015**, *55*, 745.
2. Ohta, Y.; Murase, H.; Hashimoto, T. *J. Polym. Sci. Part B: Polym. Phys.* **2005**, *43*, 2639.
3. Chodak, I. *Prog. Polym. Sci.* **1998**, *23*, 1409.
4. Liu, S.; Wang, J.; Wang, Y.; Wang, Y. *Mater. Des.* **2010**, *31*, 1711.
5. Xing, Z.; Hu, J.; Wang, M.; Zhang, W.; Li, S.; Gao, Q.; Wu, G. *Sci. Chin. Chem.* **2013**, *56*, 1504.
6. Saleem, J.; Bazargan, A.; Barford, J.; McKay, G. *Polym. Adv. Technol.* **2014**, *25*, 1181.
7. Pal, K.; Bag, S.; Pal, S. *J. Porous Mater.* **2008**, *15*, 53.
8. McCann, J. T.; Marquez, M.; Xia, Y. *J. Am. Chem. Soc.* **2006**, *128*, 1436.
9. Moon, S.; Choi, J.; Farris, R. *J. Fiber Polym.* **2008**, *9*, 276.
10. Gupta, A.; Saquing, C. D.; Afshari, M.; Tonelli, A. E.; Khan, S. A.; Kotek, R. *Macromolecules* **2009**, *42*, 709.
11. Kwon, I. K.; Kidoaki, S.; Matsuda, T. *Biomaterials* **2005**, *26*, 3929.
12. Li, N.; Xiao, C.; Mei, S.; Zhang, S. *Desalination* **2011**, *274*, 284.
13. Smook, J.; Flinterman, M.; Pennings, A. *Polym. Bull.* **1980**, *2*, 775.
14. Kalb, B.; Pennings, A. *J. Mater. Sci.* **1980**, *15*, 2584.
15. Smook, J.; Pennings, A. *J. Appl. Polym. Sci.* **1982**, *27*, 2209.
16. Hoogsteen, W.; Ten Brinke, G.; Pennings, A. *J. Mater. Sci.* **1990**, *25*, 1551.
17. Tian, Y.; Zhu, C.; Gong, J.; Yang, S.; Ma, J.; Xu, J. *Polymer* **2014**, *55*, 4299.
18. Ohta, Y.; Murase, H.; Hashimoto, T. *J. Polym. Sci. Part B: Polym. Phys.* **2010**, *48*, 1861.
19. Xiao, M.; Yu, J.; Zhu, J.; Chen, L.; Zhu, J.; Hu, Z. *J. Mater. Sci.* **2011**, *46*, 5690.
20. Yeh, J. T.; Lin, S. C.; Chen, K. N.; Huang, K. S. *J. Appl. Polym. Sci.* **2008**, *110*, 2538.
21. Chi, Z.; Chou, T. W.; Shen, G. *J. Mater. Sci.* **1984**, *19*, 3319.
22. Wang, Z.; Yu, W.; Zhou, C. *Polymer* **2015**, *56*, 535.
23. Jian, T.; Shyu, W. D.; Lin, Y. T.; Chen, K. N.; Yeh, J. T. *Polym. Eng. Sci.* **2003**, *43*, 1765.
24. Kalb, B.; Pennings, A. *Polymer* **1980**, *21*, 3.
25. Cui, K.; Meng, L.; Ji, Y.; Li, J.; Zhu, S.; Li, X.; Tian, N.; Liu, D.; Li, L. *Macromolecules* **2014**, *47*, 677.
26. Tang, Y.; Jiang, Z.; Men, Y.; An, L.; Enderle, H.-F.; Lilge, D.; Roth, S. V.; Gehrke, R.; Rieger, J. *Polymer* **2007**, *48*, 5125.
27. Strobl, G.; Schneider, M. *J. Polym. Sci. Polym. Phys. Ed.* **1980**, *18*, 1343.
28. Strobl, G.; Schneider, M.; Voigt-Martin, I. *J. Polym. Sci. Polym. Phys. Ed.* **1980**, *18*, 1361.
29. Men, Y.; Rieger, J.; Lindner, P.; Enderle, H.-F.; Lilge, D.; Kristen, M. O.; Mihan, S.; Jiang, S. *J. Phys. Chem. B* **2005**, *109*, 16650.
30. Ruland, W. *J. Appl. Crystallogr.* **1971**, *4*, 70.
31. Keum, J. K.; Zuo, F.; Hsiao, B. S. *Macromolecules* **2008**, *41*, 4766.